Unconfined slumping of a granular mass on a slope

Fukashi Maeno, Andrew J. Hogg, R. Stephen J. Sparks, and Gary P. Matson

Related Articles

Additional information on Phys. Fluids

Unconfined slumping of a granular mass on a slope

Fukashi Maeno,[1,2] Andrew J. Hogg,[3] R. Stephen J. Sparks,[1]
and Gary P. Matson[3]

[1]*School of Earth Sciences, University of Bristol, Wills Memorial Building, Queen's Road, Bristol BS8 1RJ, United Kingdom*
[2]*Earthquake Research Institute, The University of Tokyo, 1-1-1, Yayoi, Bunkyo-ku, Tokyo 113-0032, Japan*
[3]*School of Mathematics, University of Bristol, University Walk, Bristol BS8 1TW, United Kingdom*

This study investigates the gravitationally driven dynamics of dense granular materials, released from rest and allowed to flow down a slope until they stop moving. Laboratory experiments were performed in which a measured volume of material was released from rest in a cylindrical tube and spread across an unconfined rigid plane inclined at angles less than the angle of repose. Upon release, the particles initially spread outward radially. However, up-slope motion is rapidly suppressed while down-slope motion is promoted, which leads to an approximately ellipsoidally shaped deposit once the flow has been fully arrested. The flows were modeled under the shallow layer approximation and integrated numerically to capture the motion from initiation to final arrest. In modeling, two types of Coulomb-type friction models were employed. One had a constant friction coefficient, and another had a friction coefficient that depends upon the dimensionless inertial number of the motion. When the initial aspect ratio of a granular mass is small and the slope angle is low ($<5°$), the model with a constant friction coefficient can capture the shape of the deposit. However, when the slope angle is increased, the friction model that is dependent on inertial number becomes more important. For granular columns of initially high aspect ratios, the shallow water model fails to reproduce some aspects of the experimental observations. Finally, the dependence of the shape and depth of the deposit upon dimensionless parameters that characterize the system is examined under the constant friction coefficient model, demonstrating that the deduced scaling arguments are borne out by the numerical simulations and laboratory data. © *2013 American Institute of Physics*. [http://dx.doi.org/10.1063/1.4792707]

I. INTRODUCTION

Dense granular flows generated by the slumping of granular materials are often encountered in industrial processes that involve the transport and deposition of grains such as seeds, cereals, and tablets. They also occur in geophysical systems, such as pyroclastic flows caused by the collapse of a lava dome or volcanic explosions, snow avalanches, and landslides. Recently, the dynamics of granular flows caused by the slumping of a fixed mass has been studied theoretically and experimentally.[1–8] In these studies, a granular mass was instantaneously released from a cylindrical tube on a horizontal plane,[1,2] a spherical cap on an unconfined rough inclined plane,[3,4] and a box-shaped space behind a lock-gate on chutes.[5–8]

Constructing a numerical model to capture the major characteristics of spreading granular materials is a significant challenge because the mechanics of the grains and their interactions are incompletely understood at a fundamental level. One approach has been to exploit the thinness of the flows relative to their length by employing a depth-averaged description in which the flow is assumed to have a constant bulk density. Equations are developed to represent mass and momentum conservation. Previous studies[3–6,9–14] have suggested that key features, such as the variation

in thickness of deposits resulting from slumping, can be captured well by this approach. Another approach involves discrete element modeling to reproduce the motion and deposit characteristics of granular slumping onto a horizontal plane.[15–17] However, in the latter case, computational time, memory, and complexity place some limits on their application to large-scale geophysical applications. The depth-averaged approach can describe not only steady uniform granular flows in laboratory scale but also unsteady non-uniform ones on complex terrains, as encountered in the field.[18]

A key issue is the granular friction law that is introduced into depth-averaged models. This problem has been investigated for laboratory-scale granular flows but remains under debate.[4,6,12,19] A classical model for dense granular flows[5] uses a Coulomb-type friction model in which a single constant friction coefficient is adopted. Then, under the shallow water assumption and when the initial aspect ratio of a granular mass is low, this approach can approximately capture the deposit shape of a collapsing granular column on a horizontal plane.[20] For flows down an inclined plane, friction laws, which depend on flow properties, such as thickness, velocity, and grain-size, become important.[4,21]

Recent laboratory experiments and numerical simulations of dense granular flows suggest that rheology can be described by a friction coefficient, which corresponds to the ratio of the shear to normal stress. Variation of this coefficient with shear rate and pressure is captured through a dimensionless inertial number (I), defined below.[22,23] Under the shallow water assumption, however, how well this friction model works remains unclear when applied to unsteady flows. In this paper, we compare a constant friction model with a model that makes use of a friction law within the inertial number framework, and show the benefits of the latter for unconfined slumping of granular materials on slopes.

This paper is organized as follows. In Sec. II, an unsteady two-dimensional (2D) shallow layer model is formulated, in which a Coulomb-type friction model with a friction coefficient that is either constant or a function of inertial number (I) is introduced. In Sec. III, the experimental setup and observation of granular slumping on unconfined horizontal and inclined planes are reported. In Sec. IV, a shallow water model is applied to the configuration of the laboratory experiment, using the two friction models. Thus, the validity of the models is assessed. In Sec. V, the dependence of the shape and depth of the deposit upon dimensionless parameters that characterize the system is examined using the constant friction coefficient model. In Sec. VI, the main findings are discussed and summarized.

II. MODEL DESCRIPTION

The shallow layer model for dense granular flows is based upon the thickness of the flow being much less than its extent on an inclined plane, so that the acceleration perpendicular to the slope is negligible. The model is identical to previous studies,[5,10,11,24] but the handling of friction laws is somewhat different. A Cartesian coordinate system is defined in which the x-axis points down the slope and is inclined at a constant angle, θ, to the horizontal, the y-axis points across the slope, and the z-axis points upward and normal to the slope. Because of the shallowness of the flow, the pressure is given by $p = \rho g(h - z)\cos\theta$, where ρ denotes the bulk density, which is assumed constant, g is the gravitational acceleration, and h is the thickness of the flowing layer. The depth-integrated governing equations, which represent conservation of mass and momentum balance down- and cross-slope, may be written in the following form:

$$\frac{\partial h}{\partial t} + \frac{\partial}{\partial x}\int_0^h \tilde{u}\,dz + \frac{\partial}{\partial y}\int_0^h \tilde{v}\,dz = 0, \tag{1}$$

$$\frac{\partial}{\partial t}\int_0^h \tilde{u}\,dz + \frac{\partial}{\partial x}\int_0^h \tilde{u}^2\,dz + \frac{\partial}{\partial y}\int_0^h \tilde{u}\tilde{v}\,dz + \frac{\partial}{\partial x}\left(\frac{1}{2}gh^2\cos\theta\right) = gh\sin\theta - \frac{T_x}{\rho}, \tag{2}$$

$$\frac{\partial}{\partial t}\int_0^h \tilde{v}dz + \frac{\partial}{\partial x}\int_0^h \tilde{u}\tilde{v}dz + \frac{\partial}{\partial y}\int_0^h \tilde{v}^2 dz + \frac{\partial}{\partial y}\left(\frac{1}{2}gh^2\cos\theta\right) = -\frac{T_y}{\rho}, \tag{3}$$

where h is the flow thickness, $\tilde{u}$ and $\tilde{v}$ are the flow velocities in the x and y directions, respectively, (T_x, T_y) is the boundary shear stress between the flowing layer and the underlying plane, and t is the time. The velocity fields are replaced with their depth-averaged counterparts

$$vh = \int_0^h \tilde{v}dz \quad \text{and} \quad uh = \int_0^h \tilde{u}dz. \tag{4}$$

To close the model, the integrals of $\tilde{u}^2$, $\tilde{u}\tilde{v}$, and $\tilde{v}^2$ are represented in terms of depth averaged counterparts. Thus,

$$\int_0^h \tilde{u}^2 dz = \Gamma_1 u^2 h, \quad \int_0^h \tilde{u}\tilde{v}dz = \Gamma_2 uvh, \quad \text{and} \quad \int_0^h \tilde{v}^2 dz = \Gamma_3 v^2 h, \tag{5}$$

where Γ_i are shape factors that account for shear in the velocity profiles. It can be shown that $\Gamma_i \geq 1$ for all velocity profiles. However, as is common in most studies that employ the shallow layer equations, $\Gamma_i = 1$. This is an assumption that is only strictly valid when there is plug flow. Hogg and Pritchard[25] present an analysis of the effects of keeping shape factors in the governing equations and illustrate that in some fluid flows, especially close to the front where the fluid depth becomes small, the effects may be non-negligible. In Sec. IV, the effect of shape factors on final deposit shapes is examined for these granular flows. The governing equations are given by

$$\frac{\partial}{\partial t}\begin{bmatrix} h \\ hu \\ hv \end{bmatrix} + \frac{\partial}{\partial x}\begin{bmatrix} hu \\ hu^2 + \frac{1}{2}gh^2\cos\theta \\ huv \end{bmatrix} + \frac{\partial}{\partial y}\begin{bmatrix} hv \\ huv \\ hv^2 + \frac{1}{2}gh^2\cos\theta \end{bmatrix} = \begin{bmatrix} 0 \\ gh\sin\theta - T_x/\rho \\ -T_y/\rho \end{bmatrix}. \tag{6}$$

Complex processes such as effects of pore pressure have been neglected, although these are recognized as important in debris flows.[24] Recent studies are followed in assuming that the normal stresses are isotropic, so that the "earth pressure coefficient" is unity.[4,26] Then a simple Coulomb-type formulation is adopted for the basal shear stress, T, in the following form:

$$\begin{bmatrix} T_x \\ T_y \end{bmatrix} = \frac{\mu\rho gh\cos\theta}{\sqrt{u^2 + v^2}}\begin{bmatrix} u \\ v \end{bmatrix}, \tag{7}$$

where μ is a friction coefficient. In this study two different friction models are examined. One is a model with a constant angle of friction between the grains, in which the boundary has the following form:

$$\mu = \tan\delta, \tag{8}$$

where δ is the basal friction angle of the granular material. In the other model, the friction coefficient is a function of a dimensionless inertial number, I, as expressed in the following form:[22]

$$\mu(I) = \mu_s + \frac{\mu_2 - \mu_s}{I_0/I + 1}, \tag{9}$$

where I_0 is a constant that is empirically determined by experimental studies. A typical value of I_0 for glass beads is ~ 0.3 as discussed by GDR MiDi.[27] The inertial number, I, is defined as $\dot{\gamma}d/\sqrt{P/\rho_p}$, where $\dot{\gamma}$ is the shear rate (the second invariant of the deformation rate tensor), P is the confining

pressure, and d and ρ_p are the particle diameter and density, respectively.[27,28] The friction coefficient starts from a critical value of μ_s (=$\tan\delta_s$) at zero shear rate and tends to a limiting value μ_2 (=$\tan\delta_2$) at high values of I. The force balance for steady uniform flows on horizontal or inclined planes implies that the ratio between shear stress and normal stress is constant. As a result, the equation of $\mu(I)$ means that the dimensional shear rate I is constant across the layer.[22,27] The shear rate then varies with depth as the square root of the pressure (and, therefore, as the square root of the depth), because the pressure increases with depth as $P = \rho g(h - z)\cos\theta$ (with an average value $\hat{P}$ = $\rho gh\cos\theta/2$). Velocity varies as (depth)$^{3/2}$, if it is assumed that there is no-slip at the base of the flowing layer. An average velocity gradient is given by the mean velocity, $\hat{V}$, divided by the flow depth, h. So, the average of I can be estimated as

$$\hat{I} = \frac{5}{2}\frac{\hat{V}d}{h\sqrt{gh\cos\theta}},$$ (10)

where the factor 5/2 arises from the Bagnold-like velocity profile.[27] In the shallow water model, this relationship between $\hat{I}$, mean flow speed, and layer depth is used.

The above system of partial differential equations (6) is solved using a finite volume method for hyperbolic problems[29] where the first order Godunov method is incorporated to capture the discontinuous solutions appearing in the system. The basic numerical calculation procedure, especially the determination of the source term in the Eq. (6), is mostly the same as in Doyle *et al.*,[14] but we use an HLLC Riemann Solver for wet-dry dam break problems[30] instead of a Roe solver to avoid a non-physical assumption of a small amount of mass in the "vacuum" part of the flow (a "pre-wetted" layer). The dimensional grid size is 2.5 mm and the area calculated is a 800×480 grid (2 m and 1.2 m for x- and y-directions, respectively). The time step is variable and automatically selected based on a Courant number condition to ensure stability.

Stopping criteria for the granular material are introduced based on a Coulomb threshold.[11] The threshold value of the shear stress, σ_c, has the following form on an inclined plane:

$$\sigma_c = \mu\rho gh\cos\theta.$$ (11)

After solving the hyperbolic equations on the left side of Eq. (6), in which the source term on the right side is assumed to equal to zero, the admissible basal shear stress $\tilde{T}$ at the node i and time t + 1 is evaluated using the solution for [hu, hv]. Here, $\tilde{T}$ can be written in the following form:

$$\begin{bmatrix} \tilde{T}_x \\ \tilde{T}_y \end{bmatrix}_i^{t+1} = \begin{bmatrix} hu \\ hv \end{bmatrix}_i^{t+1} + \Delta t \begin{bmatrix} g\sin\theta_x h \\ g\sin\theta_y h \end{bmatrix}_i^{t+1},$$ (12)

where Δt is a time step. When $|\tilde{T}| < \sigma_c$, i.e., the basal shear stress is less than the threshold value and the flow velocity [u, v] is set to be zero. When $|\tilde{T}| > \sigma_c$, the whole system represented by Eq. (6) is solved using the basal shear stress T in Eq. (7).

III. LABORATORY EXPERIMENTS

A. Method

Dry granular material (glass ballotini with mean diameters, d, of 100 and 400 μm) was released from a cylindrical tube (with an initial radius $r_0 = 5$ cm) down a wooden plane (Fig. 1) inclined to the horizontal at angles $\theta = 0°$, 5°, 10°, and 15°. Care was taken to ensure that the particles were relatively free of any residual moisture by bubbling air through them in a fluidized bed for several minutes prior to their release. Removing surface moisture reduces cohesive effects, which could play a significant role for small particles. The initial masses of granular material, M, were 0.5, 1.0, 1.5, 2.0, and 2.5 kg, which correspond to initial aspect ratios of the granular column, here defined as the ratios of initial heights to the initial radii, $A = 0.86$, 1.7, 2.6, 3.4, and 4.3, with a measured bulk density of 1.4 g/cm^3. Granular material was poured into the tube, the top surface was carefully smoothed to ensure it was parallel with the slope, its elevation, h_0, was measured, and then the confining tube was rapidly lifted using a pneumatic trigger to initiate the flow down
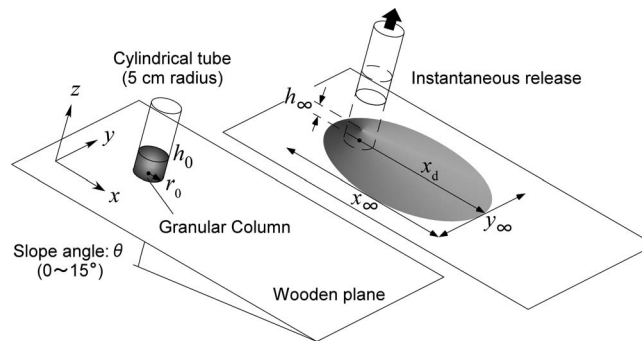
FIG. 1. Experimental configuration. The axisymmetric granular column is released by rapidly removing the confining cylindrical tube. Granular material flows down an unconfined wooden slope. Definitions of variables are shown.

the plane. Once the material had come to rest, the resulting deposit was measured to determine its perimeter. Additionally, the thickness variation, h, was measured at various locations down-slope and across-slope by carefully inserting thin pins throughout the grains so that they were minimally disturbed. Snapshots and video footage of slumping materials were taken.

A dynamic basal friction angle, δ, and the internal friction angle (repose angle), φ, of the granular material was measured in this experimental setup and the values are listed in Table I. The roughness of the wooden plane generates a dynamic friction angle that is comparable to the angle of repose of the grains and thus it is probable that the flowing layers do not simply slide over the plane without internal deformation. Lube *et al.*[1] studied collapses of granular columns on three different surfaces: a smooth wooden plane, a smooth transparent plastic plane, and a rough plane made of sand paper. They found no significant differences between the deposit shapes. This suggests that the interaction of the granular flow with the substrate makes little difference to the runout in this type of experimental configuration.

B. Observations

For slumps on horizontal planes (initial aspect ratio $A > 0.86$) the granular material initially collapsed and spread radially. Avalanching eroded the entire initial column surface leaving a conical pile. The final deposit had a steep central cone and an axisymmetric tapering frontal region (Fig. 2(a)), a result similar to other laboratory studies.[1,2]

As the slope angle is increased, the collapse and spreading behavior of the granular material is similar to that observed on a horizontal plane, but the runout distance is not axisymmetric (Figs. 2(b)–2(d)). Up-slope motion is rapidly arrested, motion down the incline is enhanced, and there is some limited cross-flow spreading, leading to an ellipsoidally shaped deposit. Enduring contact between the particles leads to frictional forces arresting the motion. These basic characteristics of the flow motion were the same for all slope angles. Small-scale surface features sometimes formed during the final phases of emplacement (Fig. 2). These may be residual features of moisture-induced cohesion and were not observed in the experiments with the larger grains.

Cross sections of deposits for up- and down-slope directions are shown in Fig. 3. The deposit shape is characterized by a peaked top, as observed in experiments on a horizontal plane. However,

TABLE I. Material properties of the granular materials: mean particle diameter d, grain density ρ_b, angle of repose φ, dynamic bed friction angle δ.

Material	d (μm)	ρ_b (g/cm^3)	φ ($^\circ$)	δ ($^\circ$)
Ballotini	70-110 (ave. 100)	2.5	23 ± 1	24 ± 1
Ballotini	400-800 (ave. 400)	2.5	22 ± 1	17 ± 1
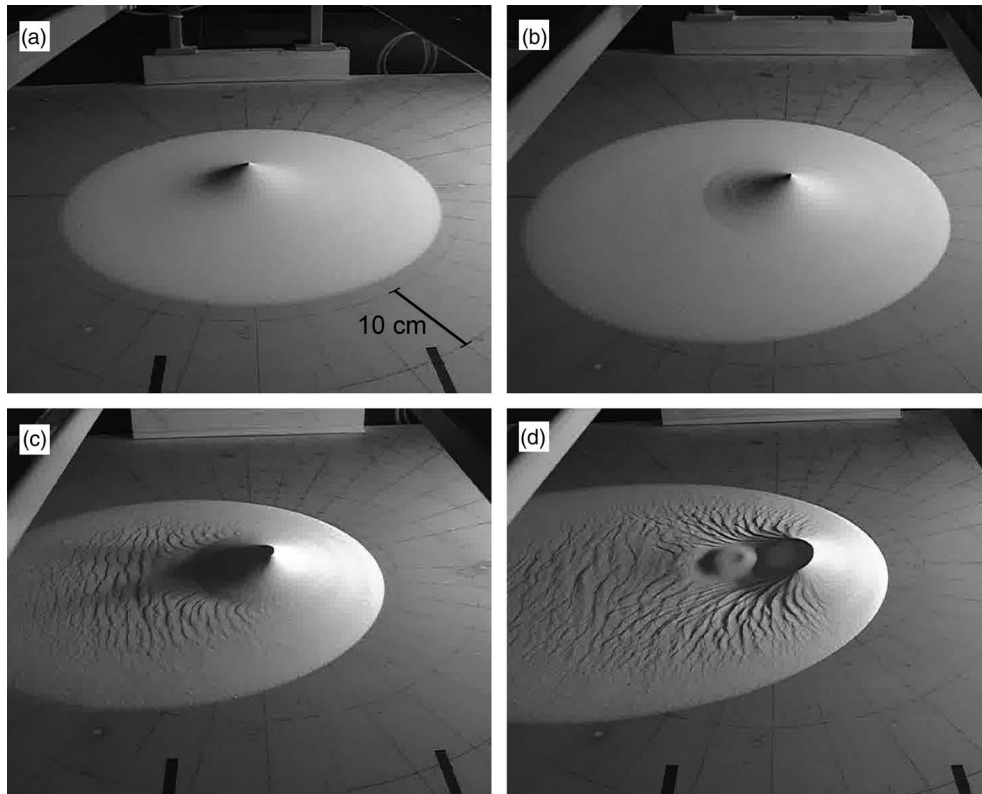
FIG. 2. Final deposit shapes for various slope angles (θ) using initial granular mass of 2.0 kg. (a) $\theta = 0°$, (b) 5°, (c) 10°, and (d) 15°. Down-slope direction is to the left.

for the cases using a 15° slope, the highest position, which is defined as h_∞, is located slightly up slope and is lowered. As a result, the deposit is characterized by a horseshoe shaped morphology defined by a semi-circular rim in the up-slope direction. This shape becomes much prominent for larger masses ($M > 1.5$ kg) as seen in Figs. 2(c) and 2(d). The runout along the centerline ($x = 0$) is systematically increased in the down-slope direction and decreased in the up-slope direction as the inclination of the plane is increased for both 100 and 400 μm diameter grains.

Variations in the perimeter of the ellipsoidally shaped deposits with mass released, M, and inclination, θ, are summarized in Fig. 4. A steep slope results in a more elongated deposit. The shape can be characterized by the ratio of the maximum width in the cross-slope direction (y_∞) to maximum extent in the down-slope direction (x_∞), which decreases systematically as the slope angle increases (Fig. 5). The maximum runout distance in the down-slope direction (x_d) systematically increases with both M (or aspect ratio, A) and θ (Fig. 6). We observe that for the granular slumps on a horizontal plane there is a small systematic divergence from the motion being purely radial, which would lead to $y_\infty/x_\infty = 1$. Measurement error of the boundary or of the inclination of the plane could account for some of this discrepancy, but we are unable to identify clearly its cause. Of much greater importance, however, is the more substantial decrease in y_∞/x_∞ as the inclination of the underlying boundary increases.

For different initial masses of granular material, the runout distance of the flow is plotted as a function of time, taking examples from a slope angle of 15° using the 100 μm grains (Fig. 7). Granular flows show a primary acceleration phase (convex downward) in the initial 0.2 s, followed by a phase of constant velocity and a final deceleration phase (convex upward). The same time-distance relationship is observed in other laboratory experiments.[1,2,7] The maximum speed is observed in the second phase, which contrasts with theoretical analyses on dam-break flows.[12,20,25]
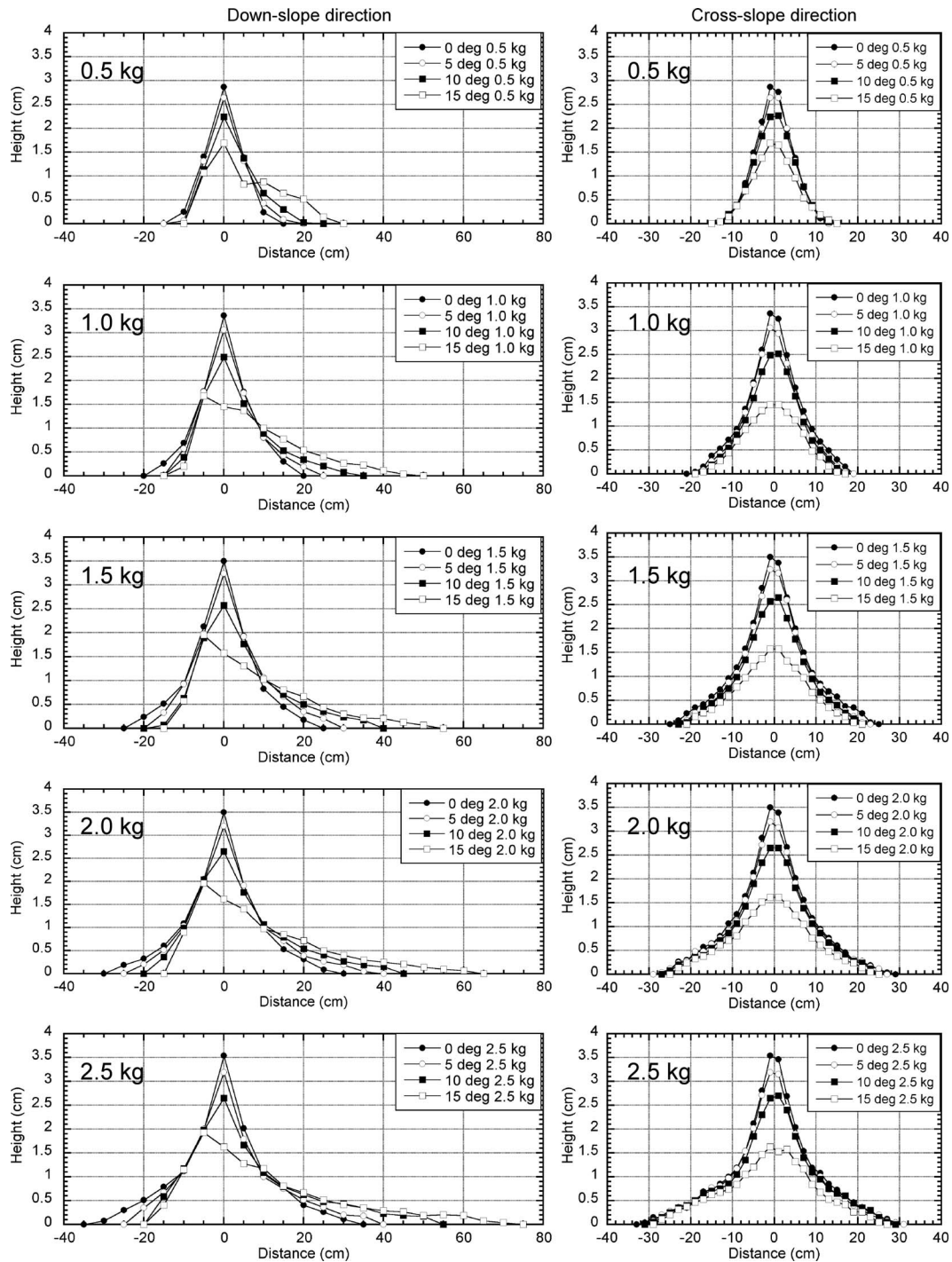
FIG. 3. Cross sections of final deposits in laboratory experiments for particles with an average diameter of 100 μm. Left: *x*-direction profile taken along the line of $y = 0$; right: *y*-direction profile taken across the line of $x = 0$. The mass in the release is given for each plot in the captions.

IV. APPLICATION OF THE MODEL TO LABORATORY RESULTS

Two different Coulomb-type friction models were applied to laboratory experiments, namely, the constant friction coefficient model and the *I*-dependent friction model. These laws require the specification of friction angles: for the Coulomb model, there is a single friction angle, δ, whereas
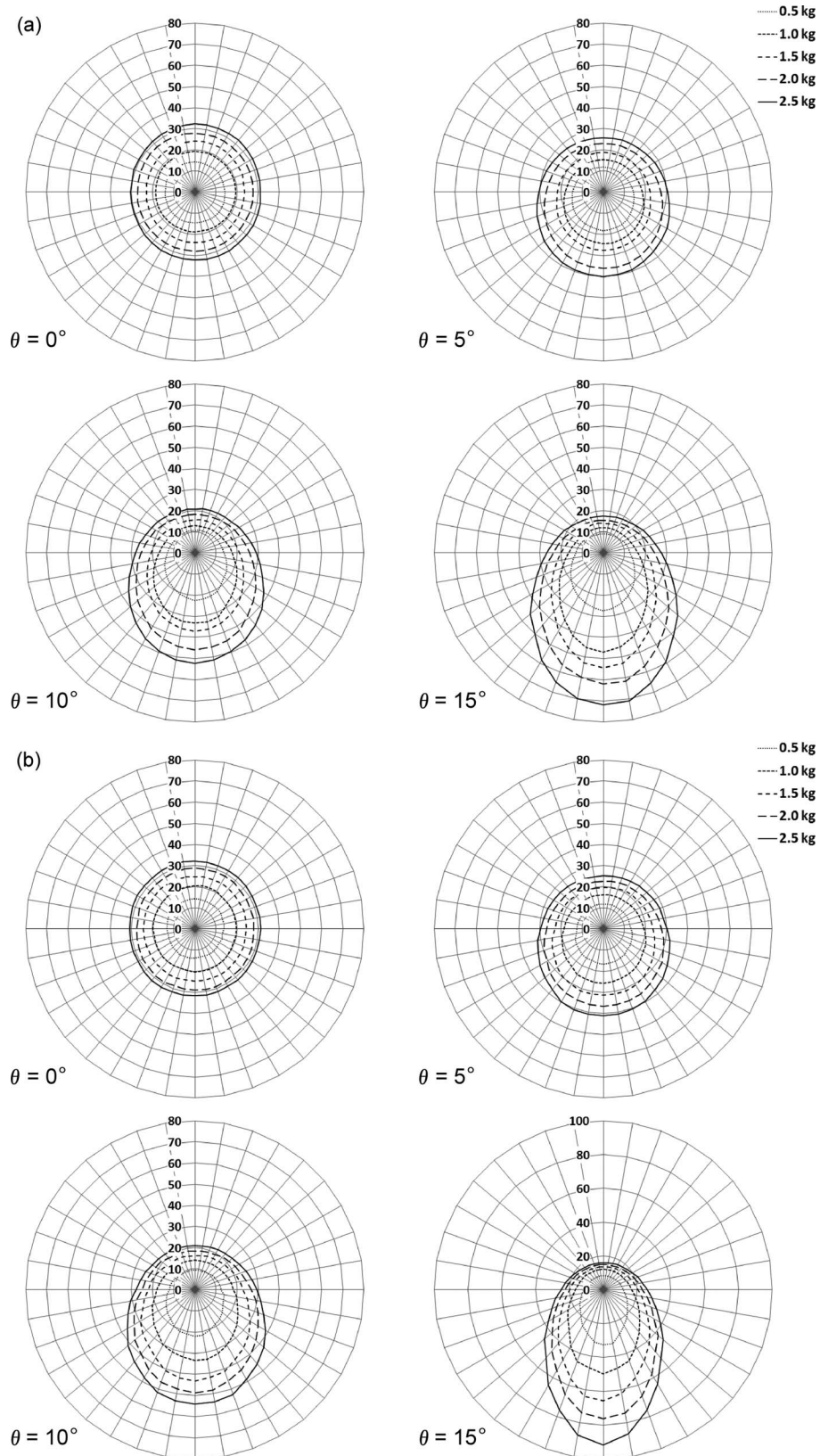
FIG. 4. Perimeter of the deposits using grains with diameters of (a) 100 μm and (b) 400 μm in laboratory experiments. Radial distances are in cm.
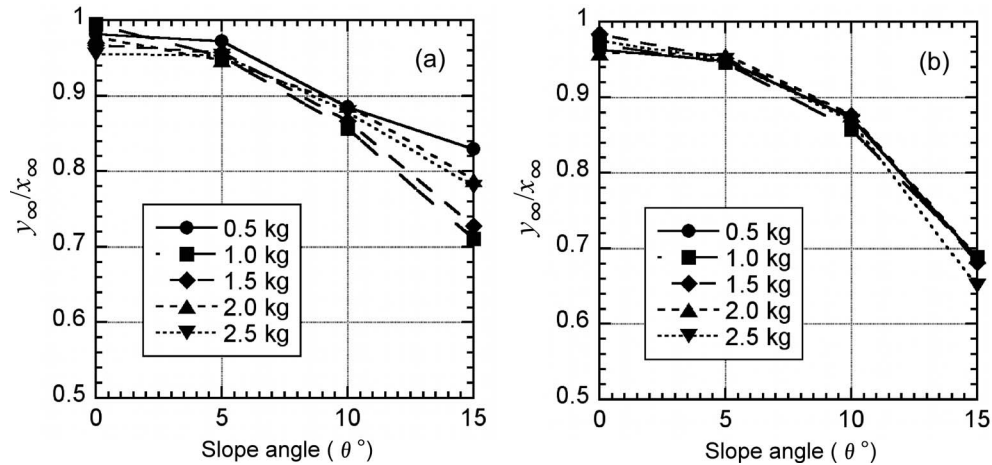
FIG. 5. The relationship between slope angle (θ) and axial ratio (y_∞/x_∞) of an elliptically shaped deposit for initial granular mass (M) with grain diameters of (a) 100 μm and (b) 400 μm.

for the I-dependent model there are two friction angles, δ_s and δ_2, as well a constant, I_0, which here is taken to be 0.3.[27] Although previous studies have suggested appropriate values for δ, δ_s, and δ_2 for glass beads (see, for example, GDR MiDi[27]), here in our numerical simulations we examine the results for a small range of friction angles spanning the previously reported values (Table II). We also examined the effects of shape factors on the distribution and extent of the deposit for slumps over a horizontal plane.

A. Horizontal plane

Numerical results show good agreement with laboratory data when the model is applied to a granular column with a low initial aspect ratio ($A = 0.86$, $M = 0.5$ kg) using a constant friction angle (δ) of 30° (Fig. 8). Although different constant friction angles ($\delta = 28°$, 30°, and 32°) were examined, $\delta = 30°$ produced the best-fit result. When the I-dependent friction law is used, where δ_s is changed over the range from 22° to 26° and δ_2 is fixed at 30°, the model predicts a longer runout distance (characterized as a perimeter) and a lower deposit height than observed.
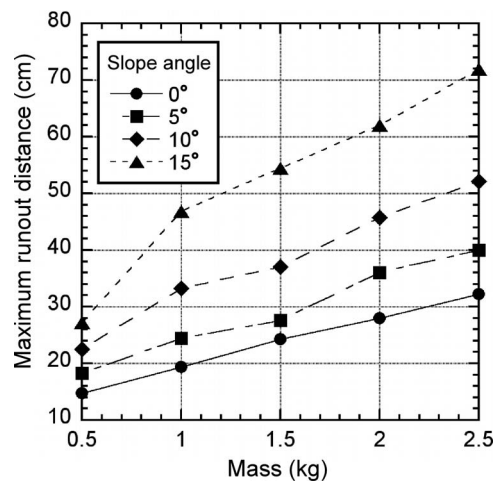
FIG. 6. The maximum down-slope runout distance (x_d) as a function of the mass of granular material released (M), for slope inclinations $\theta = 0°$ to 15°. Grain diameter is 100 μm.
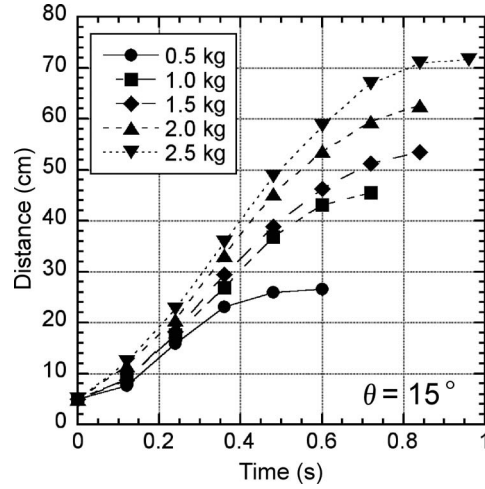
FIG. 7. A time-distance plot of the flow front position in a down-current direction for an initial mass of granular material (0.5 to 2.5 kg). Slope angle θ is 15°. Grain diameter is 100 μm.

For larger mass releases, deposit characteristics cannot be reproduced by either of the friction models; runout distance is overestimated by 10% to 20% for $M = 1.5$ kg and 20% to 35% for $M = 2.5$ kg (Fig. 8). This result indicates that the model is not applicable for high aspect ratio cases, because the initial vertical accelerations and velocities during release become significant and the confining pressure is non-hydrostatic.[1,2] When a time-distance relationship for the flow front position is plotted, the initial acceleration phase of slumping cannot be captured by the shallow water approximation.

Under Coulomb's law with a constant angle of friction, there is no velocity shear and so it is appropriate to set the shape factors, Γ_i, to unity. However, for the Pouliquen flow rule (Eqs. (9) and (10)), velocity shear is anticipated, and in its simplest form, when there is no-slip at the base, this implies that $\Gamma_i = 5/4$. The effects of the shape factors on the final deposit shapes were examined for a granular collapse on a horizontal plane.

An increase of Γ_i with a fixed friction angle ($\delta = 30°$) leads to a little more material deposited near the center of the pile and slightly increased runout, but the final shape is not very significantly affected. The range of results ($\pm 8\%$ error for the final deposit height) is approximately the same as the error caused by the uncertainty in the dynamic friction angle ($\delta = 30 \pm 2°$) (Fig. 9). Given the impossibility of measuring the velocity profiles in the experimental setup, and being unable to measure the shape factors directly, all shape factors were set to unity, noting that this approximation is applied in most shallow layer models of granular flows.[5,10,11,24]

B. Inclined planes

The quasi-elliptical shape of the deposits is largely captured by the numerical model, but a detailed comparison between observation and numerical results reveals some discrepancies in the

TABLE II. Friction angles of granular material used in numerical simulation: dynamic bed friction angle δ, minimum critical friction angle δ_s, and maximum friction angle δ_2.

Model	Friction angles (°)	
Constant friction	δ	28, 30, 32
I-dependent friction	δ_s	22, 24, 26
	δ_2	26, 28, 30, 32
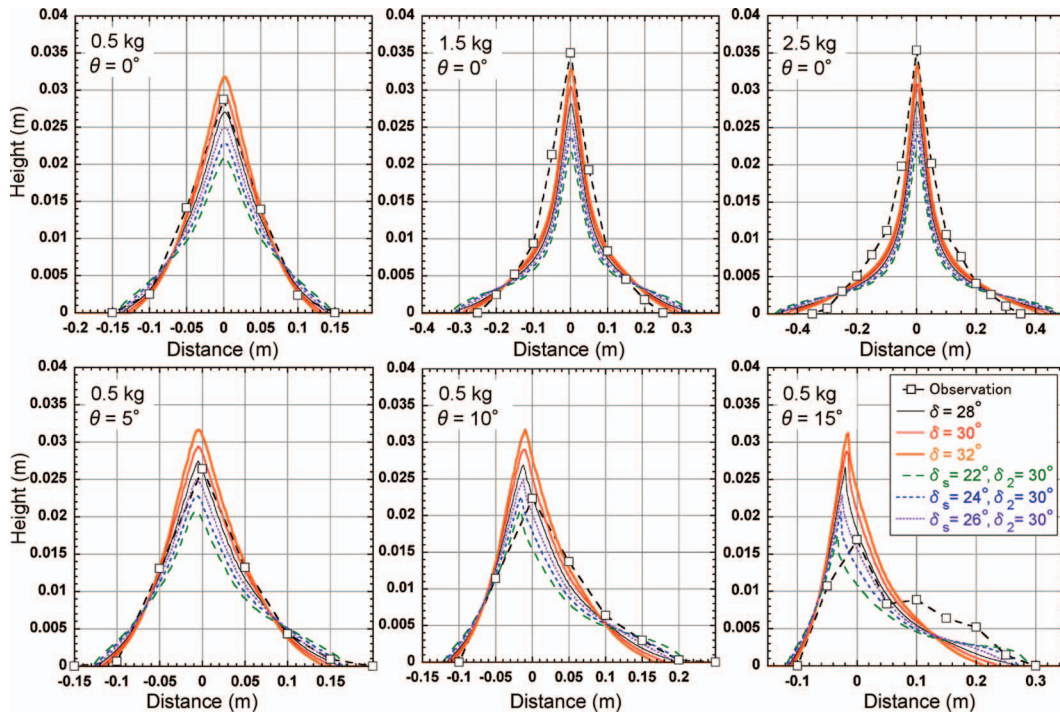
FIG. 8. Cross section of flow deposits in the x-direction from numerical simulation and observation for $M = 0.5$ kg, 1.5 kg, and 2.5 kg with $\theta = 0°$ (upper), and $M = 0.5$ kg with $\theta = 5°$, $10°$, and $15°$ (bottom). For a constant friction coefficient model, $\delta = 28°$ (thin solid line, black), $30°$ (medium solid line, red), and $32°$ (thick solid line, orange) were examined. For the I-dependent (varying friction coefficient) model (s), δ_s was set to be $22°$ (long dashed line, green), $24°$ (medium dashed line, blue), or $26°$ (short dashed line, purple) with a constant value of $\delta_2 = 30°$.

profiles of the deposits (Figs. 8, 10, and 11). For small mass releases with a low initial aspect ratio ($M = 0.5$ kg, $A = 0.86$), deposit cross sections in the x-direction produced by numerical simulation and experimental observation are compared for each slope angle and each friction model (Fig. 8). For a constant friction coefficient of $\delta = 30°$ and a slope angle of $5°$, numerical simulations overestimate the maximum deposit height, h_∞, and underestimate the runout distance, x_d, both by $\sim 20\%$. If the
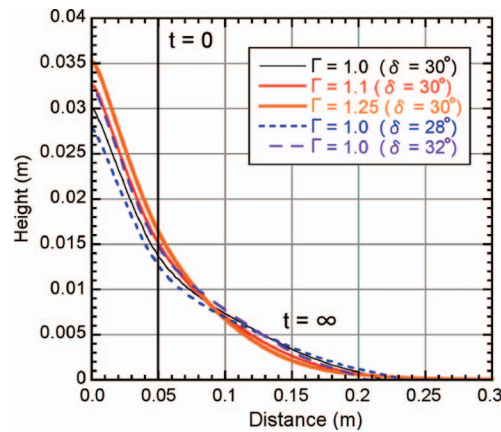
FIG. 9. The depth of the final deposit as a function of the radial distance from release for a friction angle of $30°$ and for various shape factors $\Gamma = 1.0$ (thin solid line, black), 1.1 (medium solid line, red), and 1.25 (thick solid line, orange). Also plotted are the deposit for friction angles $28°$ (short dashed line, blue) and $32°$ (long dashed line, purple) with $\Gamma = 1.0$. The initial conditions consist of a 1.0 kg mass of particles held within a cylinder of radius 5 cm. The flow was computed over a horizontal boundary.
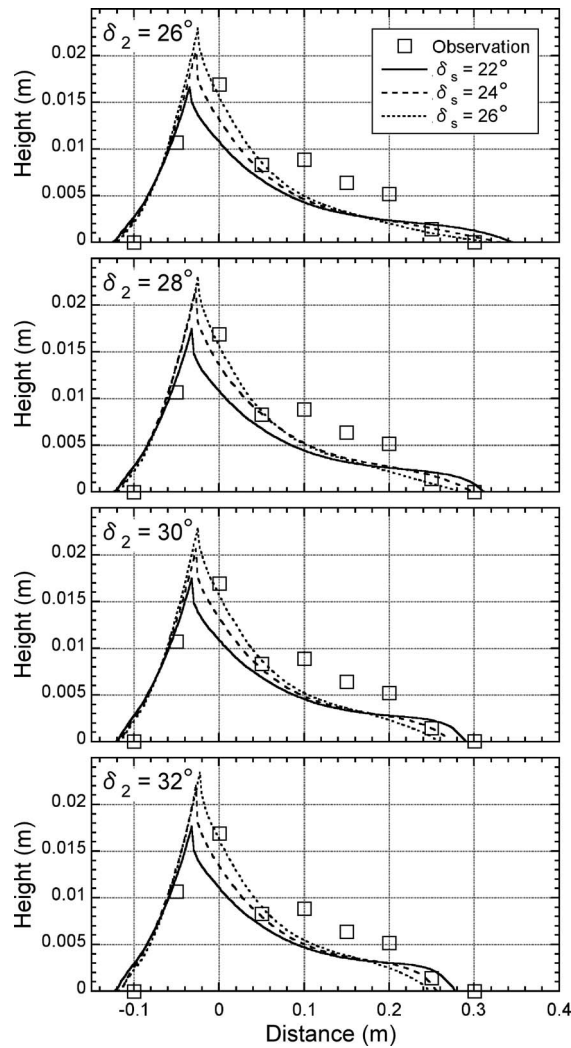
FIG. 10. Cross sections of flow deposits in the *x*-direction from observation (open squares) for $M = 0.5$ kg with $\theta = 15°$ and numerical simulation using the *I*-dependent friction model where δ_s was set to be 22° (solid line), 24° (long dashed line), or 26° (short dashed line) and δ_2 was set to be 26°, 28°, 30°, or 32°. A model with $\delta_s = \delta_2 = 26°$ is equal to a constant friction coefficient model with $\delta = 26°$.

constant friction model with $\delta = 28°$ or the *I*-dependent friction model with $\delta_s = 26°$ and $\delta_2 = 30°$ is applied, numerical results agree well with laboratory data (within 7% error for both x_d and h_∞). In the cases of $\delta_s = 22°$ and 24°, the simulation estimates x_d within 10% error but underestimates h_∞ by 15% to 20%.

With increasing slope angle, the discrepancy between the numerical simulations using the constant friction coefficient model and observation becomes more evident. The deposit height is overestimated by 20% to 40%. Results using the *I*-dependent friction model, however, are consistent with observations for steeper slopes. The lower value of $\delta_s = 22°$ gives well fitting results for 15° angle when $\delta_2 \sim 30°$, although x_d is underestimated and the central part of the down-current profile is also not well produced (Fig. 8). When different maximum friction angles ($\delta_2 = 26°$ to 32°) are used, the runout distance, x_d, is changed (Fig. 10), but the deposit height, h_∞, is only negligibly changed. (It exhibits an approximate 5% variation.) For smaller values of δ_2 (26° and 28°), a higher δ_s is required to capture the runout distance, but the deposit height cannot be reproduced simultaneously. After some tests using different friction angles (as listed in Table II), the pairing of $\delta_s = 22°$ to 24° and $\delta_2 = 30°$ to 32° gives best-fit results for the higher slope angles (Fig. 10). Then, both
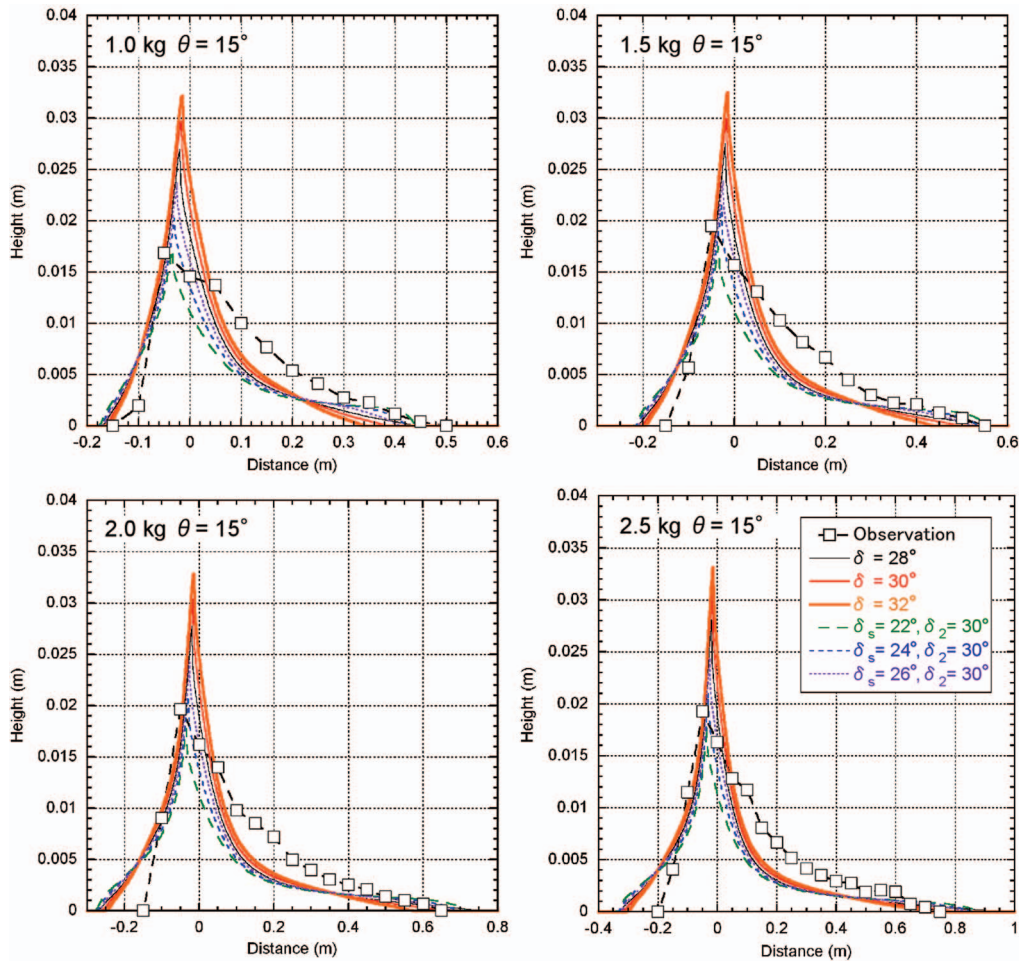
FIG. 11. Cross sections of flow deposits in the *x*-direction from numerical simulation and observation for $M = 1.0$ to 2.5 kg and $\theta = 15°$. Legend is the same as in Fig. 8.

models reproduce the observation that the runout distance in the up-slope direction decreases with an increase of slope angle (Fig. 2).

For cases using a larger mass with a higher initial aspect ratio ($M > 1.0$ kg, $A > 2$), it is difficult to reproduce the cross-sectional profiles in the experiments, although the maximum deposit height is captured by the *I*-dependent friction model. Numerical examples using a slope angle of 15° are shown in Fig. 11. Here, x_d is overestimated by ∼15% and ∼20% for 2.0 and 2.5 kg, respectively, when $\delta_s = 22°$. The central part of the down-slope profile is underestimated and difficult to reproduce in all cases. This feature also occurs at lower slope angles.

Comparison of x_d in the down-current direction for numerical simulations and laboratory observations is shown in Fig. 12. For smaller masses (<1.5 kg), the constant friction model fits the observed runout distance, x_d, for small slope angles, but the *I*-dependent model is better for steeper slopes. Simultaneously, h_∞ and its position are also consistent with observations when the *I*-dependent model is used (Fig. 8). For larger masses (2.0 and 2.5 kg), x_d is overestimated by ∼25%, even for small slope angles. The constant friction model with $\delta = 30°$ or 32° gets close to observations for larger slope angles (within 20% error), but h_∞ is overestimated by 40% to 60% (Figs. 11 and 12). The ratio of the maximum lateral extent (y_∞) to the maximum streamwise extent (x_∞) for the ellipsoidally shaped deposit decreases with the slope but it is not significantly affected by mass (Fig. 13). This relative independence upon mass of release is what was observed in the experimental results (Fig. 5). However, there are quantitative differences between the theoretical predictions and
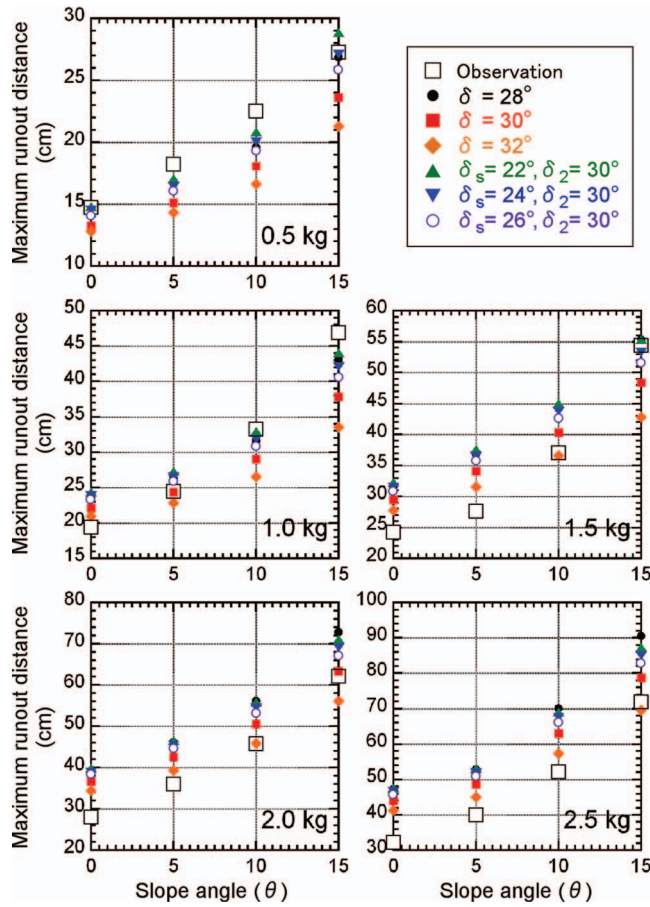
FIG. 12. Comparison of the maximum runout distance in the down-current direction for laboratory observation (open squares) and numerical simulation for a constant friction coefficient model (solid circles, solid squares, and diamonds) and the *I*-dependent model (upward/downward triangles and open circles). Colors in legend corresponding to the friction models are the same as in Fig. 8.

the experiments: for the larger slope inclinations, the differences become up to ∼20%, because the cross-slope runout is overestimated by the numerical model.

Figure 14 shows the relationship between runout time, t/t_∞, and runout distance, $(x - r_0)/x_{\rm d}$, non-dimensionalised by observation data. Here, t_∞ is the emplacement time of the granular flows. The numerical simulations do not capture the initial acceleration phase. The speed of the major
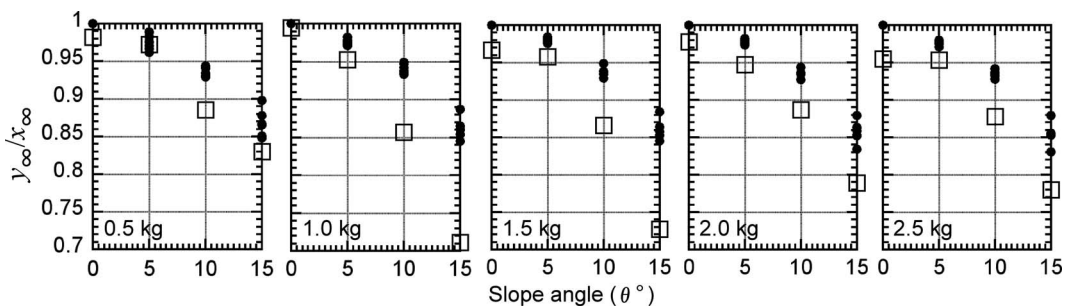
FIG. 13. Relationships between slope angle (θ) and axial ratio (y_∞/x_∞) for elliptically shaped deposit consisting of different initial granular mass (*M*). Open squares are laboratory data; closed circles are numerical results for two different friction models using different friction angles.
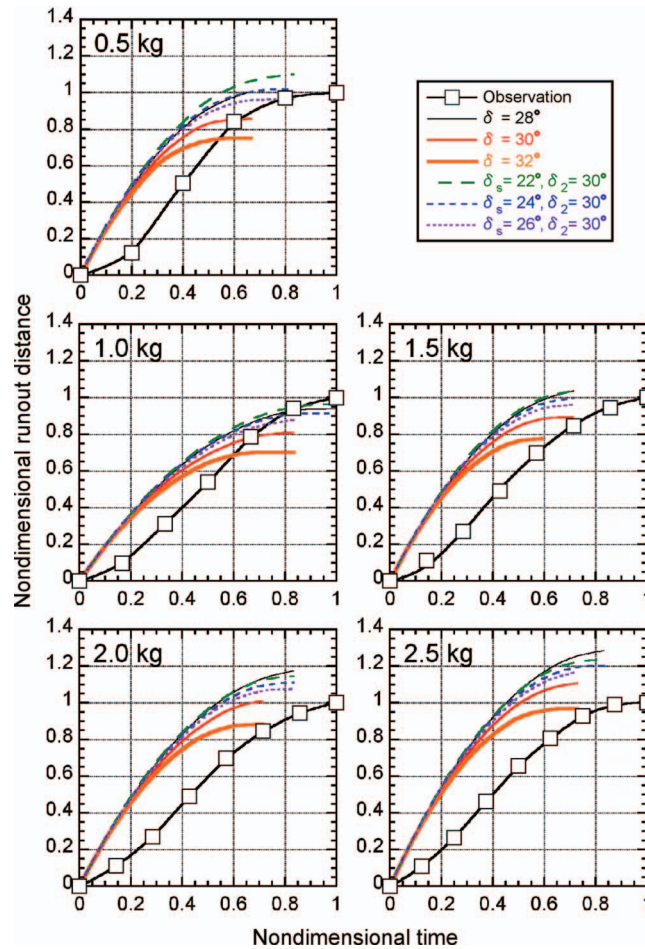
FIG. 14. Comparison of time-distance plots of the flow front position in the down-current direction. Initial mass of granular material is 0.5 to 2.5 kg). Slope angle θ is 15°. A non-dimensional distance and non-dimensional time scale are used. They are normalized by the maximum runout distance and the duration of flow observed in laboratory experiments, respectively. Legend is the same as in Fig. 8.

propagation phase is consistent with observations after about 0.2 s for different friction models and friction angles. Previous numerical and analytical studies also failed to capture the initial phase.[12, 20, 25] This is explained by the shallow water approximation not being appropriate during the initial phases of the collapse when there is non-negligible vertical acceleration as the material slumps upon release.

C. Effects of friction models

The I-dependent friction model gives an increasingly better fit to deposit shapes as slopes increase. A major difference between the two friction models is apparent in the x-direction profile. The laboratory deposits have a steeply curved front and are reproduced by only the I-dependent friction model (Fig. 15).

The distribution and extent of the deposit produced from releases of initially small aspect ratios are well reproduced by the numerical model with typical mismatches of less than 10% in the predicted depth and extent. In Fig. 16, representative numerical results, using the best fit parameters for releases with $M = 0.5$ kg, are shown for each slope angle. With an increase of slope angle, which causes a longer runout distance, the model requires a lower friction angle of δ_s to reproduce the experimental measurements. By choosing a best-fitting values of friction angle, δ_s, which is close
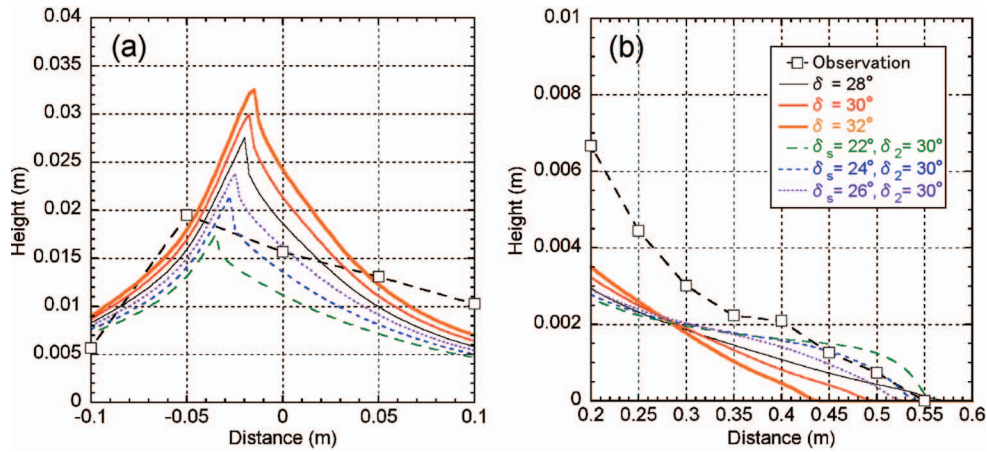
FIG. 15. Magnification of cross section (*x*-direction) in the central (a) and the frontal (b) parts of the deposit from numerical simulation and observation ($M = 1.5$ kg, $\theta = 15°$). For the maximum deposit height, h_∞, the *I*-dependent friction model (especially with $\delta_s = 22°$ and $24°$) shows a better agreement with observation than the constant friction coefficient model does. The frontal shape is also reproduced well by the *I*-dependent model. Legend is the same as in Fig. 8.

to $22°$ (a typical value for glass beads[4,31]), we find that we can produce quite good quantitative agreement between the theoretical predictions and experimental observations, although the cross-slope runouts are slightly overestimated. Figure 16 shows contours of the deposit and illustrates the emergence of a crescent (or "horseshoe") feature in the deposit as the inclination of the slope is increased (see Fig. 2).
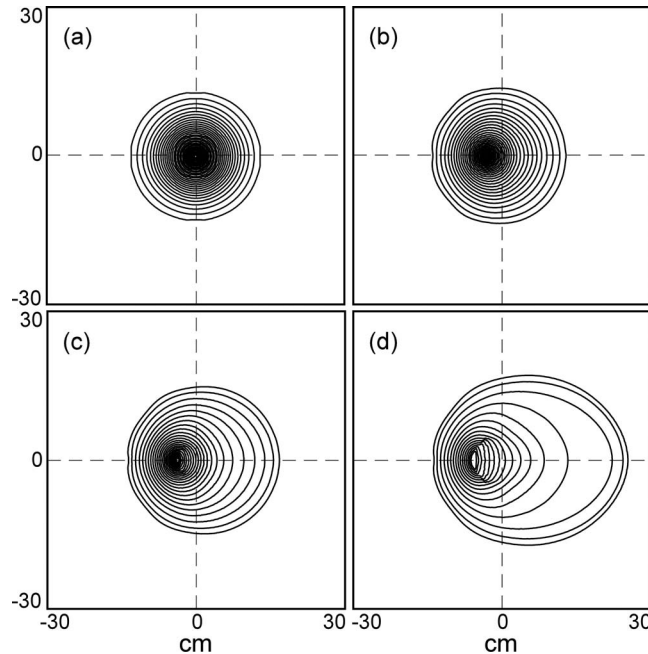
FIG. 16. Results of numerical simulation using $M = 0.5$ kg (initial column radius is 5 cm) on unconfined slopes. (a) $\theta = 0°$, constant friction model ($\delta = 30°$), (b) $\theta = 5°$, *I*-dependent friction model ($\delta_2 = 30°$, $\delta_s = 26°$), (c) $\theta = 10°$, *I*-dependent friction model ($\delta_2 = 30°$, $\delta_s = 24°$), (d) $\theta = 15°$, *I*-dependent friction model ($\delta_2 = 30°$, $\delta_s = 22°$). Contour interval is 1 mm.

V. SCALING ANALYSIS

The dependence of the shape and depth of the deposit upon dimensionless parameters that characterize the system is now examined. For this analysis and for simplicity, only the Coulomb model of basal drag with a constant coefficient of friction, $\mu = \tan\delta$, is investigated with numerical simulations run over a wide range of initial condition and slope inclinations. We anticipate that broadly similar results as those that follow could be produced for the *I*-dependent model of friction, but this is not analyzed here to ease the exposition. The following two dimensionless ratios are defined:

$$\varepsilon = \frac{r_0\,(\mu - \tan\theta)}{h_0} \quad \text{and} \quad \lambda = \frac{r_0\mu}{h_0}, \tag{13}$$

where r_0 and h_0 are the initial radius and height of the cylinder of granular materials. Therefore, $h_0/r_0\,(=A)$ is the initial aspect ratio.

A rescaled version of the governing equations can then be introduced by defining

$$\{x, y, t, h, u, v\} = \big\{\lambda^{-1/3}r_oX,\ \lambda^{-1/3}r_oY,\ \lambda^{-2/3}r_o\,(g\cos\theta h_0)^{-1/2}\,T,$$
$$\lambda^{2/3}h_0H,\ \lambda^{1/3}\,(g\cos\theta h_0)^{1/2}\,U,\ \lambda^{1/3}\,(g\cos\theta h_0)^{1/2}\,V\big\}. \tag{14}$$

The governing equations are then given by

$$\frac{\partial}{\partial T}\begin{bmatrix} H \\ HU \\ HV \end{bmatrix} + \frac{\partial}{\partial X}\begin{bmatrix} HU \\ HU^2 + \frac{1}{2}H^2 \\ HUV \end{bmatrix} + \frac{\partial}{\partial Y}\begin{bmatrix} HV \\ HUV \\ HV^2 + \frac{1}{2}H^2 \end{bmatrix} = \begin{bmatrix} 0 \\ -\frac{\varepsilon}{\lambda}H + H\left(1 - U/\sqrt{U^2 + V^2}\right) \\ -H\left(V/\sqrt{U^2 + V^2}\right) \end{bmatrix}, \tag{15}$$

subject to the initial condition $H = \lambda^{-2/3}$ when $X^2 + Y^2 < \lambda^{2/3}$. The only parameter appearing in the governing equations is ε/λ, while λ is also in the initial conditions. The ratio ε/λ, which represents the ratio of the net down-slope drag to the cross-slope drag, is expected to play a significant role in determining the shape of the deposit. To this end, the aspect ratio of the final deposit, here defined as the ratio of its maximum width (y_∞) to its maximum length (x_∞), is plotted as a function of ε/λ (Fig. 17). This plot shows that an approximately universal curve can be obtained from the numerical model with the deposit varying from approximately circular with $\varepsilon \cong \lambda$, to being extended far down slope when $\varepsilon/\lambda \ll 1$. In this plot $0.12 < \lambda < 0.72$ and $0.05 < \varepsilon < 0.72$ and the fact that the numerical data clusters quite closely around a single curve when plotted as a function of ε/λ illustrates that the
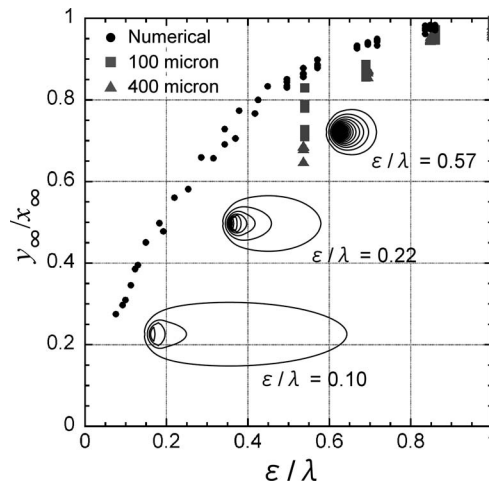
FIG. 17. The shape of the final deposit, characterized by the ratio of its cross-slope to down-slope extent, y_∞/x_∞, as a function of ε/λ. Circles show numerical data. Squares and triangles show experimental data with 100 and 400 μm-diameter grains, respectively, assuming $\delta = 30°$. Typical deposit profiles at some values of ε/λ.

aspect ratio of the deposit, y_∞/x_∞, depends only weakly on λ, which appears in the initial conditions, but much more strongly on ε/λ, which appears in the governing equation. The experimental data is also overlain on this plot and follows the same basic trends as in the numerical data, but with some differences, as detailed in Sec. IV. In particular, the scatter in the experimental points at ε/λ $= 0.54$ just corresponds to the scatter in the points at $\theta = 15°$ (Fig. 5(a)). In this section, we focus on attempting to explain the numerically computed variation of y_∞/x_∞ and the final depth of deposit relative to the initial depth (h_∞/h_0) with the dimensionless parameters ε and λ.

The scaling analysis described below follows results derived by Hogg[6] for 2D slumps down slopes, a study which provided a theoretical basis for some of the deductions for large aspect ratio slumps made by Lajeunesse *et al.*[2] and Kerswell.[12] The analysis is based on the regime $\varepsilon \ll \lambda \ll 1$, so that frictional effects are relatively weak and the slope relatively steep, thus extending the deposit far down slope. However, as found for 2D slumps, the scaling results work rather robustly even in regimes far outside their domain of validity.

Initially the granular material slumps and spreads radially, with its motion driven by a balance between the radial pressure gradient and its inertia, before being progressively affected by friction and down-slope acceleration. Eventually, friction overcomes the driving forces and the material is arrested. Cross-slope spreading is inhibited first since down-slope friction is compensated by a component of gravitational acceleration. The scales for the depth of the granular slump can be determined during each phase by applying and modifying the analysis developed by Hogg.[6] First, during the initial radial spreading, the radius increases linearly with time, $R = \lambda^{-1/3}T$, where the radial velocity is related to the square root of the initial height of the release. Then since mass is conserved $H \sim 1/R^2$ and thus we deduce that the depth can be described by $H \sim \lambda^{2/3}/T^2$ (cf. Hogg[6]). Friction becomes important for the cross-slope momentum balance when the inertia and pressure gradient are of comparable magnitude. This demands $\partial V/\partial T \sim \partial H/\partial Y \sim 1$. Thus, similar to Hogg,[6] we deduce that since $V \sim Y/T$, friction is non-negligible when $Y \sim T^2$, $H/Y \sim 1$, and so $H \sim \lambda^{1/3}$. In terms of the original dimensional variables, the depth when cross-slope spreading is inhibited is given by $h/h_0 \sim \lambda$. Subsequently, the granular material continues to flow, but its motion is now predominantly down slope. The depth of the material is therefore scaled as $H \sim \lambda^{1/3}/T$, because in this regime the cross-slope motion is inhibited, but the down-slope motion remains as $X \sim \lambda^{-1/3}T$. Final arrest occurs when there is a subsequent balance between inertia, pressure gradient, and friction in the down-slope momentum equation. This requires $\partial U/\partial T \sim \partial H/\partial X \sim \varepsilon/\lambda$ and thus following Hogg[6] $H \sim \lambda^{2/9}(\varepsilon/\lambda)^{2/3}$ is deduced. In terms of the original dimensional variables, $h_\infty/h_0 \sim \lambda^{2/9}\varepsilon^{2/3}$.

These scaling predictions can now be tested against the numerical simulations. When the flow has arrested, the maximum depth of the deposit is plotted, scaled by the initial height of the released cylinder of granular material as a function of λ (Fig. 18(a)) or as a function of $\lambda^{2/9}\varepsilon^{2/3}$ (Fig. 18(b)). The simulations span a range of values of ε/λ from ~0.2 to unity, and in these figures, those with ε/λ greater than and less than 0.5 are distinguished from each other by different symbols. The scaling analysis above requires that $\varepsilon/\lambda \ll 1$ for which $h_\infty/h_0 \sim \lambda^{2/9}\varepsilon^{2/3}$ is deduced. However, when $|1 - \varepsilon/\lambda| \ll 1$ the motion is anticipated to be predominantly radial and thus $h_\infty/h_0 \sim \lambda$. There is good support (Fig. 18) for both of these scalings from the numerical simulations; the arbitrary division of the numerical data by $\varepsilon/\lambda > 0.5$ and $\varepsilon/\lambda < 0.5$ appears to work well.

The scaling analysis can also be applied to the laboratory data. When $h_\infty/h_0 \sim \lambda$ is examined for the deposit depth, there is some residual dependence upon ε/λ (Fig. 18(a)). The laboratory data with $\varepsilon/\lambda \sim 1$ are consistent with the relationship seen in the numerical results ($\varepsilon/\lambda > 0.5$), but as anticipated this relationship no longer holds as ε/λ decreases. However, when the regime $\varepsilon/\lambda \ll 1$ is examined, for which $h_\infty/h_0 \sim \lambda^{2/9}\varepsilon^{2/3}$, all the laboratory data are scaled in the same dimensionless grouping and appear to follow the predicted scaling (Fig. 18(b)). However, the gradient of the linear relationship is not the same as the numerical results (Fig. 18(b)).

Assessing the runout length scales through scaling analysis is more difficult than estimating the depths,[6] because the motion at the front may not be influenced by the motion in the bulk part of the flow where motion stops first. However, it is possible to estimate the length scales such that mass is conserved during each phase of the motion. Thus, for radial spreading, given that the height is given by $h_\infty/h_0 \sim \lambda$, the cross-slope length scale is deduced to be $y_\infty/r_0 \sim \lambda^{-1/2}$. When there is significant down-slope spreading, given that $h_\infty/h_0 \sim \lambda^{2/9}\varepsilon^{2/3}$ and $y_\infty/r_0 \sim \lambda^{-1/2}$, the down-slope
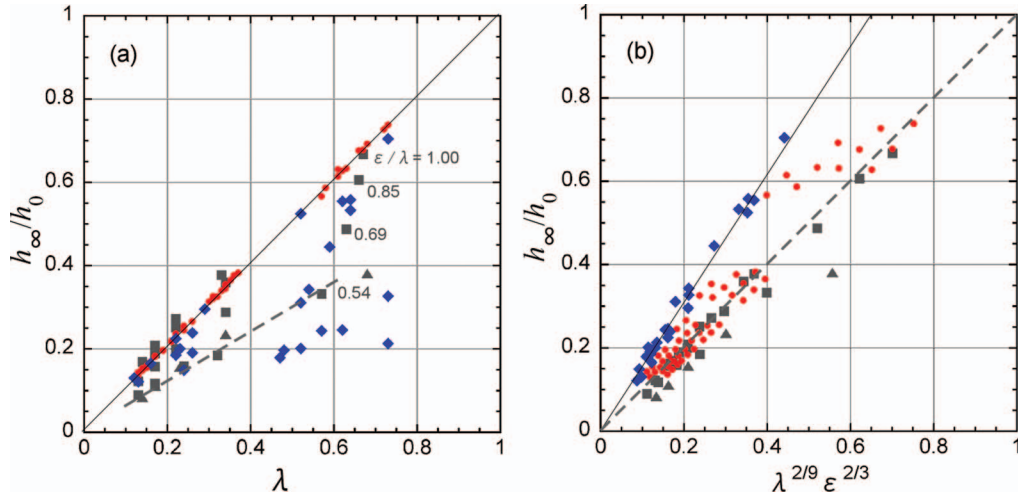
FIG. 18. (a) h_∞/h_0 as a function of λ. (b) h_∞/h_0 as a function of $\lambda^{2/9}\varepsilon^{2/3}$. Circles (red) for $\varepsilon/\lambda \geq 0.5$ and diamonds (blue) for $\varepsilon/\lambda < 0.5$ for numerical results. Squares and triangles (gray) show laboratory data with 100 and 400 μm-diameter grains, respectively, assuming $\delta = 30°$. Some of the data are indicated with values of ε/λ. Solid lines indicate the scaling relationships for numerical results, and broken lines indicate the scaling relationship for laboratory data.

length scale is found to be $x_\infty/r_0 \sim \lambda^{5/18}\varepsilon^{-2/3}$. Hence, the aspect ratio of the deposit is evaluated as $y_\infty/x_\infty \sim \lambda^{-1/9}(\varepsilon/\lambda)^{2/3}$ (Fig. 19). There is reasonable evidence of this behavior when $\varepsilon/\lambda \ll 1$ in the data from the numerical simulations. Also plotted in Fig. 19 is the laboratory data, which may exhibit a similar scaling relationship although the laboratory data may include measurement errors and the range of ε/λ examined is relatively small. It is also noteworthy that the gradient of the scaling relationships in Fig. 19 is not the same for both the numerical and experimental results.

To summarize, the scaling relationships between the deposit thickness (h_∞) and the shape (y_∞/x_∞) of the deposit with appropriate combinations of the dimensionless parameters (ε and λ) are reasonably supported well by the numerical simulations in the two regimes of substantial down-slope spreading $\varepsilon/\lambda \ll 1$ and radial motion $\varepsilon/\lambda = O(1)$. Furthermore, the arbitrary division of $\varepsilon/\lambda > 0.5$
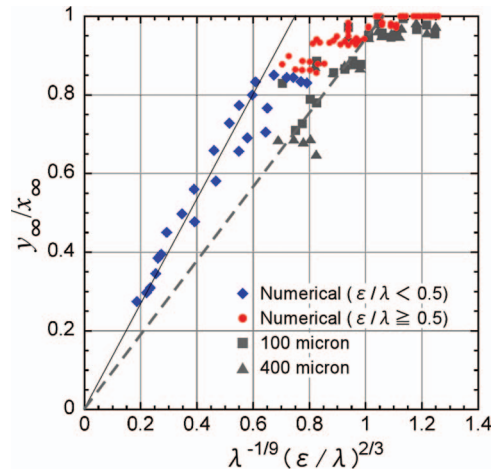
FIG. 19. y_∞/x_∞ as a function of $\lambda^{-1/9}(\varepsilon/\lambda)^{2/3}$. Circles (red) for $\varepsilon/\lambda \geq 0.5$ and diamonds (blue) for $\varepsilon/\lambda < 0.5$ for numerical results. Squares and triangles (gray) show experimental data with 100 and 400 μm-diameter grains, respectively, assuming $\delta = 30°$. Solid line indicates the scaling relationship for numerical results with $\varepsilon/\lambda < 0.5$. Broken line indicates the scaling relationship for laboratory data.

and $\varepsilon/\lambda < 0.5$ appears to capture each of the regimes. The apparent success of the scaling analysis in identifying the variations exhibited by the experiments indicates that the sequence of initially radial motion followed by arrest in the cross-slope, and then finally arrest in the down-slope direction, may occur rather generally for our release conditions. The criterion for separating the numerical simulations ($\varepsilon/\lambda > 0.5$), however, may not be more generally applicable. The shallow layer model with a constant friction has been shown to overestimate h_∞ and y_∞/x_∞, especially on steeper slopes (Figs. 8 and 13) and this may account for the different gradients in the plots for the numerical and experimental data (Figs. 18(b) and 19).

VI. DISCUSSION AND SUMMARY

This study has investigated the dynamics of dense granular materials, released from rest and allowed to flow down a slope driven by gravitational forces and then coming to rest due to the action of frictional forces. On release, the granular material initially spreads out radially, but up-slope motion is rapidly arrested and motion down the incline is promoted, leading to a quasi-ellipsoidal deposit once the flow has been fully arrested. The ratio of the across-slope to down-slope extents (y_∞/x_∞) decreases systematically as the slope angle θ increases. These results share the same characteristics for both experiments using 100 and 400 μm-diameter grains. Numerical simulations using 2D shallow water models can capture aspects of this motion as well as the distribution of the final deposits. The comparison of laboratory and numerical results indicates that for these unsteady flows, the gross characteristics of such deposits can be predicted by the models. The models, however, overestimate the ratio of the cross-slope to down-slope extents for steeper slopes (Figs. 13 and 17). This result is the same for both types of friction model using different friction angles. Contributing significantly to this consistent overestimation is that the models overestimate the runout distance in the cross-slope direction (y_∞). Pouliquen and Forterre[4] examined similar situations in laboratory experiments where the granular material was released from a spherical cap onto inclined planes and they also reported that the runout distance in the cross-slope direction is overestimated when a depth-averaged flow model is applied. There are some plausible reasons for this. First, it has been assumed that the normal stress tensor is isotropic – but this was not directly measured in these experiments and the signature of anisotropy could be an over-prediction of cross-slope runout. Further, the shallow layer model cannot capture the internal processes of granular flows, such as a growing, static, basal layer, which was suggested to play an important role in the experiments performed by Lube *et al.*[1] Also, during the initial collapse, non-hydrostatic effects will play a role on the horizontal component of flow and these might cause for the discrepancy. However, it is noteworthy that for extended and relatively shallow flows down inclined planes, the basal layer is likely to be less important than for flows over horizontal planes. Moreover, slumps down slopes extend much further and flow in a relatively shallow state for a much greater proportion of their time. Thus, it appears appropriate to employ a shallow water model for these flows during much of their evolution, while their use during the very initial phases may be questionable.

The differences between the two different friction models are noticeable. In the case of a low aspect ratio ($A = 0.78$) granular mass on a low angle slope ($\theta \leq 5°$), the constant friction model ($\delta = 28°$ to $30°$) is better at capturing the granular flow motion and deposit characteristics. When the slope θ increases, the flow is able to run down a much greater distance. Numerical results for steeper slopes indicate that an *I*-dependent friction model produces results that are more compatible with observations than a constant friction model, in terms of the final deposit shape, although there is a discrepancy in the thickness profile. The friction angles of δ_2 ($30°$ to $32°$) and δ_s ($22°$ to $24°$) used in this situation are broadly in accord with previously measured properties for glass beads.[4,27,31] Considering these observations and comparisons, under the shallow water approximation, we conclude that it appears to be more important to include a flow-dependent friction angle for predictions on steeper slopes. Presumably, this reflects the observation that when the slope is relatively steep, but still less than the friction angle so that the flows arrest, the motion has extended periods during which the velocity is constant and thus close to the truly steady regimes in which the *I*-dependent friction law was developed.

The importance of a variable friction coefficient in the shallow water model has been discussed previously in the context of a velocity-dependent friction coefficient.[4,19] Experimental observations suggest that this type of friction law will play an important role in characterizing the morphological features of granular deposits.[31,32] Most studies have focused on steady flows for slope angles higher than the angle of friction of granular material. Our study investigated the situation on unconfined slopes with lower slope angles ($0°$ to $15°$). The *I*-dependent friction model works well, although a constant friction model is still useful for capturing some aspects of unsteady granular flows. This observation may be useful for situations in which there is a range of grain sizes. In this case, it may be difficult to employ the *I*-dependent model because the model requires the specification of the local grain size, which even if it is represented by a local average, may vary spatially and temporally. The interplay between the segregation of material of different sizes and granular mobility appears to be an important topic for future investigation.

ACKNOWLEDGMENTS

[1] G. Lube, H. E. Huppert, R. S. J. Sparks, and M. A. Hallworth, "Axisymmetric collapses of granular columns," J. Fluid Mech. **508**, 175 (2004).

[2] E. Lajeunesse, A. Mangeney-Castelnau, and J. P. Vilotte, "Spreading of a granular mass on a horizontal plane," Phys. Fluids **16**, 2371 (2004).

[3] J. M. N. T. Gray, M. Wieland, and K. Hutter, "Gravity-driven free surface flow of granular avalanches over complex basal topography," Proc. R. Soc. London, Ser. A **455**, 1841 (1999).

[4] O. Pouliquen and Y. Forterre, "Friction law for dense granular flows: Application to the motion of a mass down a rough inclined plane," J. Fluid Mech. **453**, 133 (2002).

[5] S. B. Savage and K. Hutter, "The motion of a finite mass of granular material down a rough incline," J. Fluid Mech. **199**, 177 (1989).

[6] A. J. Hogg, "Two-dimensional granular slumps down slopes," Phys. Fluid **19**, 093301 (2007).

[7] N. J. Balmforth and R. R. Kerswell, "Granular collapse in two dimensions," J. Fluid Mech. **538**, 399 (2005).

[8] G. Lube, H. E. Huppert, R. S. J. Sparks, and A. Freundt, "Granular column collapses down rough inclined channels," J. Fluid Mech. **675**, 347 (2011).

[9] R. P. Denlinger and R. M. Iverson, "Flow of variably fluidized granular masses across three-dimensional terrain: 2. Numerical predictions and experimental tests," J. Geophys. Res. **106**(B1), 553, doi:10.1029/2000JB900330 (2001).

[10] E. B. Pitman, C. C. Nichita, A. Patra, A. Bauer, M. Sherian, and M. Bursik, "Computing granular avalanches and landslides," Phys. Fluids **15**, 3638 (2003).

[11] A. Mangeney-Castelnau, J. P. Vilotte, M. O. Bristeau, B. Perthame, F. Bouchut, C. Simeoni, and S. Yerneni, "Numerical modelling of avalanches based on Saint Venant equations using a kinetic scheme," J. Geophys. Res. **108**, 2527, doi:10.1029/2002JB002024 (2003).

[12] R. R. Kerswell, "Dam break with Coulomb friction: A model for granular slumping?" Phys. Fluids **17**, 057101 (2005).

[13] E. Larrieu, L. Staron, and E. Hinch, "Raining into shallow water as a description of the collapse of a column of grains," J. Fluid Mech. **554**, 259 (2006).

[14] E. E. Doyle, H. E. Huppert, G. Lube, H. M. Mader, and R. S. J. Sparks, "Static and flowing regions in granular collapses down channels: Insights from a sedimenting shallow water model," Phys. Fluids **19**, 106601 (2007).

[15] R. Zenit, "Computer simulations of the collapse of a granular column," Phys. Fluids **17**, 031703 (2005).

[16] L. Staron and E. J. Hinch, "Study of the collapse of granular columns using 2D discrete-grains simulation," J. Fluid Mech. **545**, 1 (2005).

[17] L. Lacaze, J. C. Phillips, and R. R. Kerswell, "Planar collapse of a granular column: Experiments and discrete element simulations" Phys. Fluids **20**, 063302 (2008).

[18] R. P. Denlinger and R. M. Iverson, "Granular avalanches across irregular three-dimensional terrain: 1. Theory and computation," J. Geophys. Res. **109**, F01014, doi:10.1029/2003JF000085 (2004).

[19] A. Mangeney, F. Bouchut, N. Thomas, J. P. Vilotte, and M. O. Bristeau, "Numerical modeling of self-channeling granular flows and of their levee-channel deposits," J. Geophys. Res. **112**, F02017, doi:10.1029/2006JF000469 (2007).

[20] A. Mangeney-Castelnau, F. Bouchut, J. P. Vilotte, E. Lajeunesse, A. Aubertin, and M. Pirulli, "On the use of Saint-Venant equations for simulating the spreading of a granular mass," J. Geophys. Res. **110**, B09103, doi:10.1029/2004JB003161 (2005).

[21] O. Pouliquen, "Scaling laws in granular flows down rough inclined planes," Phys. Fluids **11**, 542 (1999).

[22] P. Jop, Y. Forterre, and O. Pouliquen, "A constitutive law for dense granular flows," Nature (London) **441**, 727 (2006).

[23] Y. Forterre and O. Pouliquen, "Flows of dense granular media," Annu. Rev. Fluid Mech. **40**, 1 (2008).

[24] R. M. Iverson and R. P. Denlinger, "Flow of variably fluidized granular masses across three-dimensional terrain: 1. Coulomb mixture theory," J. Geophys. Res. **106**(B1), 537, doi:10.1029/2000JB900329 (2001).

[25] A. J. Hogg and D. Pritchard, "The effect of hydraulic resistance on dam-break and other shallow inertial flows," J. Fluid Mech. **501**, 179 (2004).

[26] D. Ertas, G. S. Grest, T. H. Halsey, D. Levine, and E. Silbert, "Gravity-driven dense granular flows," Eur. Phys. Lett. **56**, 214 (2001).

[27] GDR MiDi, "On dense granular flows," Eur. Phys. J. E **14**, 341 (2004).

[28] F. Da Cruz, S. Eman, M. Prochnow, J.-N. Roux, and F. Chevoir, "Rheophysics of dense granular materials: Discrete simulation of plane shear flows," Phys. Rev. E **72**, 021309 (2005).

[29] R. J. Leveque, "Finite volume methods for hyperbolic problems," *Cambridge Texts in Applied Mathematics* (Cambridge University Press, Cambridge, 2002).

[30] E. F. Toro, *Riemann Solvers and Numerical Methods for Fluid Dynamics* (Springer-Verlag, Berlin, 1999).

[31] G. Felix and N. Thomas, "Relation between dry granular flow regimes and morphology of deposits: Formation of levees in pyroclastic deposits," Earth Planet. Sci. Lett. **221**, 197 (2004).

[32] S. Deboeuf, E. Lajeunesse, O. Dauchot, and B. Andreotti, "Flow rule, self-channelization, and levees in unconfined granular flows," Phys. Rev. Lett. **97**, 158303 (2006).